JOURNAL OF AIRCRAFT
Vol. 41, No. 2, March–April 2004

High-Order Essentially Nonoscillatory Schemes for Rotary-Wing Wake Computations

Nathan Hariharan*
United Technologies Research Center, East Hartford, Connecticut 06018
and
Lakshmi N. Sankar†
Georgia Institute of Technology, Atlanta, Georgia 30332-0150

The use of fifth-seventh-order spatially accurate, essentially non-oscillatory (ENO) schemes for capturing vortices using Euler/Navier–Stokes equations is discussed. These schemes are constructed to minimize numerical dissipation and are evaluated for their application to flowfields laden with vorticity. The fifth-order ENO scheme is compared with a commonly used third-order MUSCL scheme for a two-bladed rotor in hover. Based on the results, the fifth- and seventh-order ENO schemes are evaluated for their ability to convect a vortex generated from a wing tip. The relative merits of these schemes for capturing vortex wakes arising from wings and rotor blades are summarized.

Nomenclature

$A(), E(), R()$	=	operators
$\|A\|$	=	Roe's dissipation matrix
C_T	=	thrust coefficient
$\boldsymbol{F}$	=	flux vector for inviscid fluxes
$\boldsymbol{F}_v$	=	flux vector for viscous fluxes
M_{tip}	=	tip Mach number (for rotor blade)
M_∞	=	freestream Mach number
$\boldsymbol{q}$	=	vector of primitive flow variables
$\boldsymbol{q}_L$	=	left-hand-side flow vector at a given face
$\boldsymbol{q}_R$	=	right-hand-side flow vector at a given face
R	=	rotor disk radius
V_F	=	fluid velocity
V_G	=	grid velocity
v_i	=	induced velocity
α	=	angle of attack
ΔS	=	face surface area
λ	=	advance ratio
τ	=	time
Ω	=	rotor angular velocity
Ω_J	=	cell volume

Introduction

THE flowfield around a rotor, whether in forward flight or hover, is difficult to model due to the presence of strong vorticity. The flow phenomena for a rotor differ from that for a wing in forward flight because of the differing influence of their respective wakes. For a wing in forward flight, the generated tip vortex and the vortex sheet are quickly convected away from the wing, and the influence of the shed wake on the flowfield in the vicinity of the wing is small. For an adequate numerical simulation of a wing in forward flight, it is sufficient to capture the generated tip vortex in the vicinity of the wing. In contrast, in the flowfield around a rotor, the strong vortex wake system lingers in the vicinity of the rotor. In hover, the strong tip vortex coils beneath the rotor and significantly alters the effective angle of attack of the rotor.

Received 3 July 2000; revision received 15 December 2002; accepted for publication 27 December 2002.

*Senior Engineer/Systems.
†Regents Professor, School of Aerospace Engineering. Associate Fellow AIAA.

Accurate numerical prediction of aerodynamic parameters such as thrust coefficient and induced torque coefficient requires an accurate modeling of the tip vortex. In forward flight, the entire vortex system is swept back, leading to strong interaction between blade-tip vortices with successive blades, a phenomenon known as the blade–vortex interaction (BVI). These BVIs result in rapid changes in local flow conditions and are a major source of aerodynamic noise and structural vibration.

The underlying issue in modeling these flows is the necessity to account for fully the complex vortex system generated by the rotor. Researchers in the past two decades have adopted a broad class of methodologies with various levels of complexity to model the vortex system. Until recently, this representation was externally input from empirical/analytical models because full Euler/Navier–Stokes (N–S) computations were infeasible. With the enormous advances in computational methodologies and computational power, researchers have been adapting Euler/N–S techniques for the study of the rotor flowfield. These solvers are particularly useful in analyzing new or complex rotor blades where no experimental data are available. Studies by Srinivasan and Ahmad,[1] Strawn and Barth,[2] and Duque[3,4] have used a variety of strategies such as unstructured methodologies and overset methodologies to tackle this problem. An excellent survey article by McCroskey[5] gives a comprehensive review of modern computational strategies for rotor applications.

Methodologies that solve for the flowfield from the basic conservation laws without using additional information (information from analyses such as other numerical formulations, analytical formulations, or experimental observations) are generally referred to as first-principles-based methods. Traditional low-order, spatially accurate Euler/N–S computational methodologies tend to dissipate the vortex wake system due to the high numerical dissipation inbuilt in such numerical schemes.[5] Some amount of dissipation is essential for numerical schemes to damp high-frequency oscillations. However, such a procedure should not diffuse legitimate flow features, such as vorticity, that exhibit sharp gradients in flow properties.

One of the earliest, relatively successful, attempts to build a high-fidelity, low numerical dissipation, high-order scheme adopted essentially nonoscillatory (ENO)[6–8] methodologies order to capture three-dimensional rotary-wing vortex wakes. In recent years, various other approaches to building high-order schemes for rotor wake capturing have also been proposed. Schemes such as Dispersion Relation Preserving (DRP) schemes[9] and projected MUSCL[10] have been tried for studying rotorcraft wakes with varying degrees of success. Compact high-order schemes, that is, schemes that use information only from any given cell and its neighbors, such as discontinuous Galerkin (see Ref. 11) have been only moderately successful for three-dimensional unsteady vortex capturing so far. More

research is needed to refine high-order methods further to arrive at an optimal scheme applicable for three-dimensional calculations.

This paper focuses upon the use of fifth-seventh-order spatially accurate, ENO schemes for capturing vortices while minimizing numerical dissipation. The fifth-order ENO scheme is compared with a commonly used third-order MUSCL scheme for a two-bladed rotor in hover. For a rotor-blade wake, the motion of the tip vortex makes it difficult to ensure that the tip vortex stays in areas of high grid point density while constraining to a relatively low overall number of grid points (~200,000 grid points). Therefore, based on the rotor–blade results, the fifth- and seventh-order ENO schemes are evaluated for their ability to convect a vortex generated from a wing tip. For the study of wing-tip vortex, the necessary grid system can be more easily constructed to ensure that the tip vortex always stays within areas of high grid point density. The relative merits of these schemes for capturing vortex wakes arising from wings and rotor blades are summarized.

High-Order Methods for Accurate Prediction of the Wake

The discretized form of the three-dimensional, unsteady finite volume version of the N–S equation was solved:

$$\frac{\partial}{\partial t}(\boldsymbol{q}\Omega_J) + \sum_{i=1}^{6}[(\boldsymbol{V}_F - \boldsymbol{V}_G)\boldsymbol{q} + \boldsymbol{F}]\cdot\Delta S = \sum_{i=1}^{6}\boldsymbol{F}_v\cdot\Delta S \qquad (1)$$

The preceding formulation allows for arbitrary motion of the grids. The temporal discretization is implemented using a three-point stencil, and the solution update process uses a Newton iterative solver to achieve third-order temporal accuracy. The viscous fluxes are computed using central differences. The inviscid fluxes are updated using an approximate Riemann solver, that is, the numerical flux on the cell faces is given by

$$\boldsymbol{F} = [\boldsymbol{F}_1(\boldsymbol{q}_L) + \boldsymbol{F}_1(\boldsymbol{q}_R)]/2 - |A|(\boldsymbol{q}_R - \boldsymbol{q}_L) \qquad (2)$$

Fifth-Seventh-Order ENO Scheme

The fifth-seventh-high order formulation for N–S solution has been developed along the lines of ENO methods developed originally by Harten et al.[6] The higher-order reconstruction comes in the projection stage of the conservative variable, that is, $\boldsymbol{q}_L$ and $\boldsymbol{q}_R$. For a smoothly varying function, these projections are based on the support stencils shown in Fig. 1a.

The details of the implementation are provided elsewhere.[7,8] The formulation is briefly discussed next for completeness. The high-order reconstruction for a three-dimensional flowfield solution is broken down as three independent one-dimensional reconstructions in the three computational dimensions. Such a breakdown keeps the overall computing efforts within a manageable limit while retaining a large portion of the benefits of the high-order reconstruction. The high-order ENO reconstruction in a single dimension is described next.

For a one dimensional initial boundary-value problem, the system of hyperbolic conservation laws may be written as

$$\boldsymbol{q}_t + \nabla f(\boldsymbol{q}) = 0, \qquad \boldsymbol{q}(x,0) = \boldsymbol{q}_0(x) \qquad (3)$$

The updated solution at the next time step, $n+1$, can be written as

$$\boldsymbol{q}_j^{n+1} = A(C_j)E(\tau)R(x;\boldsymbol{q}^n) \qquad (4)$$

Here, $\boldsymbol{q}$ are the cell-averaged state variables, R is the reconstruction polynomial approximation of the actual solution over the cell, constructed using the available cell averages, E is the evolution operator that advances the solution by a given time step, and A is the averaging operator over cell C_j to get back the cell averages at the next time step. The high-order reconstruction can either be directly applied to the fluxes themselves or to the cell-averaged state variables before using those values to compute the fluxes. In this work, the second approach was used. The high-order construction was applied to the state variables, and the approximate Riemann solver was used

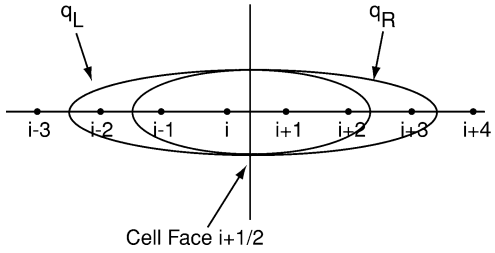

Fig. 1a Fifth-order stencils for computing left and right primitive variables.

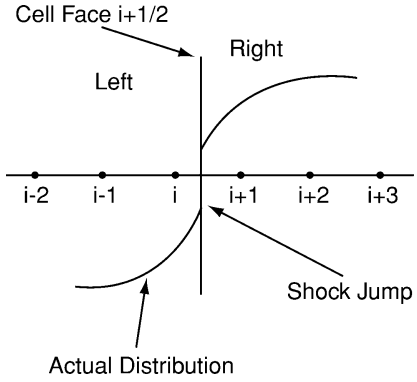

Fig. 1b Distribution with a discontinuity.

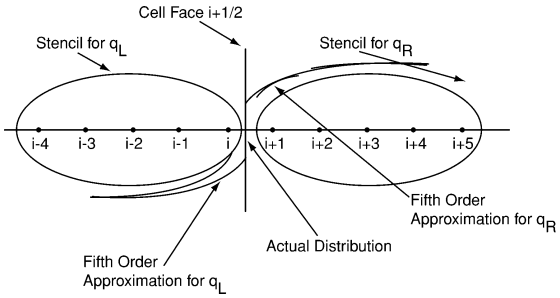

Fig. 1c Adaptive stencil for uniformly high order solution.

as the evolution operator. The fifth-order reconstruction is done as follows.

Let $\boldsymbol{J}(i)$ be the vector containing the stencil index for the ith grid point and C_j the cell associated with node j. Given the cell averages $\boldsymbol{q}_j$ of a function $q'(x)$, we need reconstruction R such that

$$R(x;q) = q'(x) + \mathcal{O}(h^r), \qquad A(C_j)R(x;\boldsymbol{q}) = q_j, \qquad j \in \boldsymbol{J}(i) \qquad (5)$$

where r is the required order of accuracy. The polynomial R can be expressed as a Taylor expansion around the centroid of cell i:

$$R_i(x;q) = \sum_{k=0}^{i=1}\frac{1}{k!}(x-c_i)^k D_k, \qquad D_k = \frac{\partial^k q'}{\partial x^k}(c_i) + \mathcal{O}(h^{r-k}) \qquad (6)$$

The D_k may be evaluated by

$$A(C_j)R_j = q_j, \qquad j \in \boldsymbol{J}(i) \qquad (7)$$

This yields a system of equations for the D_k,

$$\sum_{k=0}^{i=1} a_{j,k}D_k = q_j, \qquad j \in \boldsymbol{J}(i)$$

$$a_{j,k} = \frac{1}{k!}A(C_j)(x-c_i)^k = \frac{1}{k!|C_j|}\int_{C_j}(x-c_i)^k\,\mathrm{d}V$$

$$|C_j| = \int_{C_j}\mathrm{d}V \qquad (8)$$

Inverting the preceding system, the D_k are determined. Using these values of D_k, then R can be constructed using Eq. (6).

An economic stencil adapting strategy is adopted in the implementation. For a fifth-order scheme, there are five possible stencil variations that will include cell i, for either $\boldsymbol{q}_L$ or $\boldsymbol{q}_R$. For a smooth flow, the most symmetric stencil (with an upwind directional bias of half a cell) is preferred. In the present implementation, the stencil to be used for each point is stored. In the case of a smooth flow, the stencil pattern is set once after the flow solver is initiated. In the case of unsteady flow with shocks, the stencil adaptation is done throughout all of the domains at every so many time steps (typically every 10 time steps). At every grid point, the stencil to be used is decided by comparing a weighted absolute value of the derivatives as

$$D_{\text{sum}} = \sum_{k=0}^{i=1} \alpha_k |D_k| \tag{9}$$

The derivatives are weighted by factors α_k. The weighting factors are set to give a hierarchical preference to the most centered stencil (most preferred), followed by slightly one-sided stencil, and finally to the most one-sided stencil (least preferred), in the regions where flow properties are smooth. Such a preference will rule out wild oscillations of the stencil due to minor changes in the derivatives at every time step. This will ensure that unless discontinuities are encountered in the flowfield the centered stencil is preferred. In case a discontinuity is present in the sampling region, that is, as shown in Fig. 1b, the sampling stencils are automatically shifted to avoid sampling across the discontinuity, as shown in Fig. 1c.

The time stepping is done in an implicit manner using directional factorization.[12] A third-order Newton iterative scheme is used to integrate in time. The temporal update was done using a three point temporal stencil, that is,

$$\frac{\partial}{\partial t}(\boldsymbol{q}^{n+1}) \cong \frac{(3\boldsymbol{q}^{n+1} - 4\boldsymbol{q}^{n} + \boldsymbol{q}^{n-1})}{2\Delta\tau} + \mathcal{O}(\Delta\tau^2) \tag{10}$$

The seventh-order ENO scheme is constructed along similar lines. A wider stencil, as shown in Fig. 2, is used for the left and right projection. The stencil shifting near the boundaries and discontinuities is similar to the fifth-order implementation.

Results and Discussions

Simulation of Caradonna–Tung[13] Rotor in Hover

Grid System and Boundary Conditions

A two-bladed rotor tested by Caradonna and Tung[13] is chosen in this effort. The rotor blades are untwisted and are made up of NACA0012 sections, with an aspect ratio of 6.5. This test case has been simulated widely including first-principles-based N–S computations (see Ref. 14). The objective of this effort was to compare the fifth-order ENO (ENO-5) scheme with the third-order MUSCL solution. Of interest are the rotor-blade loads and the fidelity of the captured wake-vortex system.

An H grid was generated to capture the wake system. Figure 3 shows the H grid consisting of a lower and an upper block and the various boundary conditions that are applied. The flow properties at the interface between the upper and lower blocks are updated explicitly as an average of the interior field points immediately above and below the interface were applied. The H grid is generated over only one blade and spans 180 deg in the azimuthal direction. The flowfield is assumed to be symmetric from blade to blade, and the periodic boundary conditions account for the presence of the other blade, by taking the flowfield value at $\Psi = 0$ deg and feeding it back into the domain through $\Psi = 180$ deg.

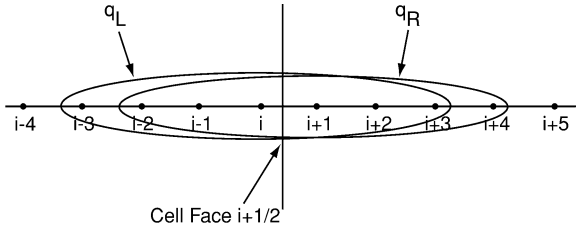

Fig. 2 Seventh-order stencil for smooth flow conditions.

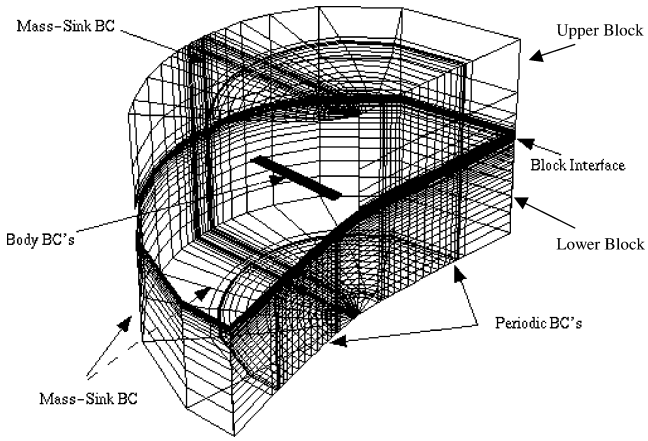

Fig. 3 H-grid system, and application of various boundary conditions for a two-bladed rotor in hover.

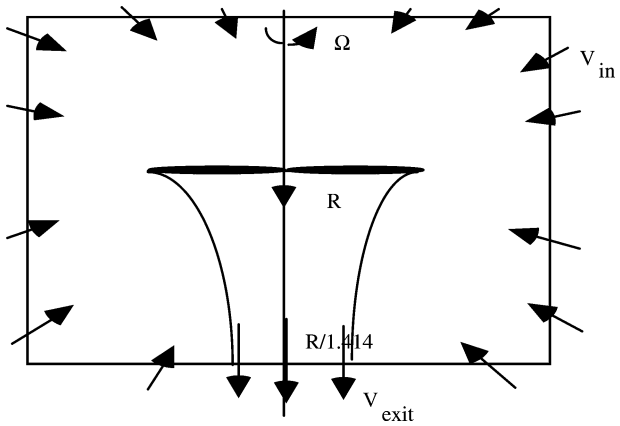

Fig. 4 Schematic of far-field inflow/outflow boundary conditions based on one-dimensional momentum.

In hover, the far-field boundary conditions are sometimes replaced by the so-called mass-sink boundary conditions.[14] The mass-sink boundary conditions are based on one-dimensional momentum theory. In this approach an exit/inlet velocity at the boundaries as a function of the thrust coefficient, radius, and the tip Mach number is prescribed, as follows. An inflow sink velocity is to be applied at the far-field boundaries,

$$V^*_{\text{sin}\,k} = (M_{\text{tip}}/4)\sqrt{C_T/2}\left[R^2/r^2(x_i)\right] \tag{11}$$

and an equivalent mass flow rate is allowed to leave the bottom boundary on an area of one-half the rotor plane,

$$V^*_{\text{source}} = V_{\text{exit}} = 2V^*_i = 2M_{\text{tip}}\sqrt{C_T/2} \tag{12}$$

This is shown schematically in Fig. 4. These velocities are not applied at the periodic boundary planes.

Surface Pressure Distributions

The initial objective was to compare the surface pressure distributions computed by the ENO-5 scheme and the third-order MUSCL scheme with experiments. The lower grid block, for this study, had 73 points in the streamwise direction, 31 points in the radial direction, and 42 points in the normal direction. The upper block had $73 \times 31 \times 22$. grid points with 22 points in the direction normal to the rotor disk. On the airfoil, there were only 20 points in the streamwise direction. The grid was rapidly stretched in the streamwise

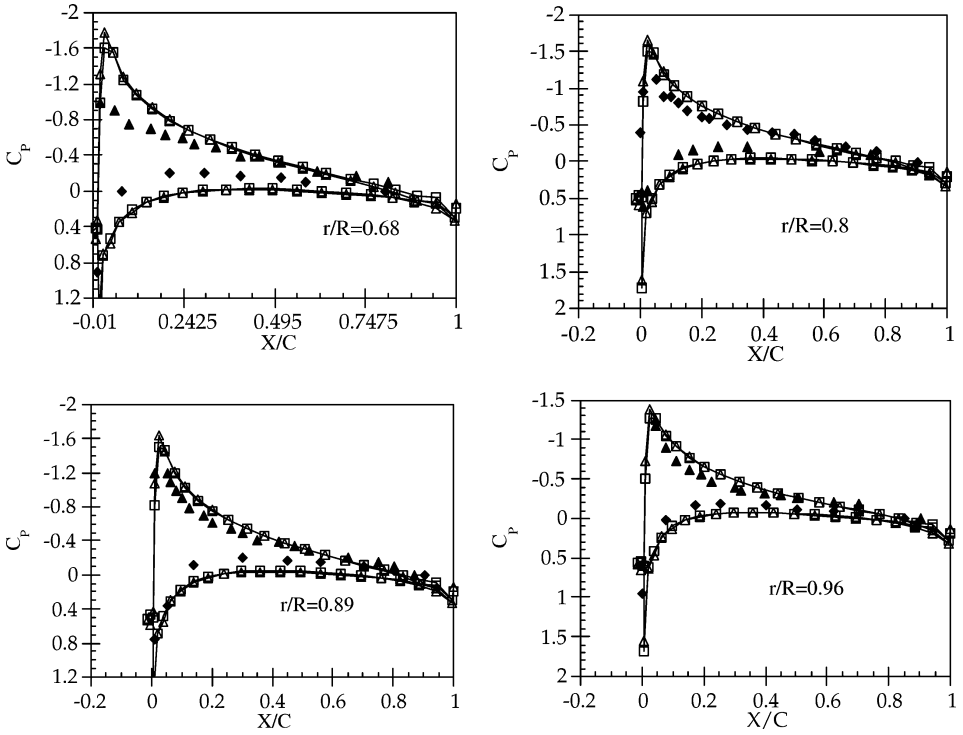

Fig. 5a Comparison of surface pressure distributions at various radial stations for the Caradonna–Tung[13] rotor-blade: □, Euler MUSCL; △, Euler Roe–ENO-5; and ◆ and ▲, experiments.

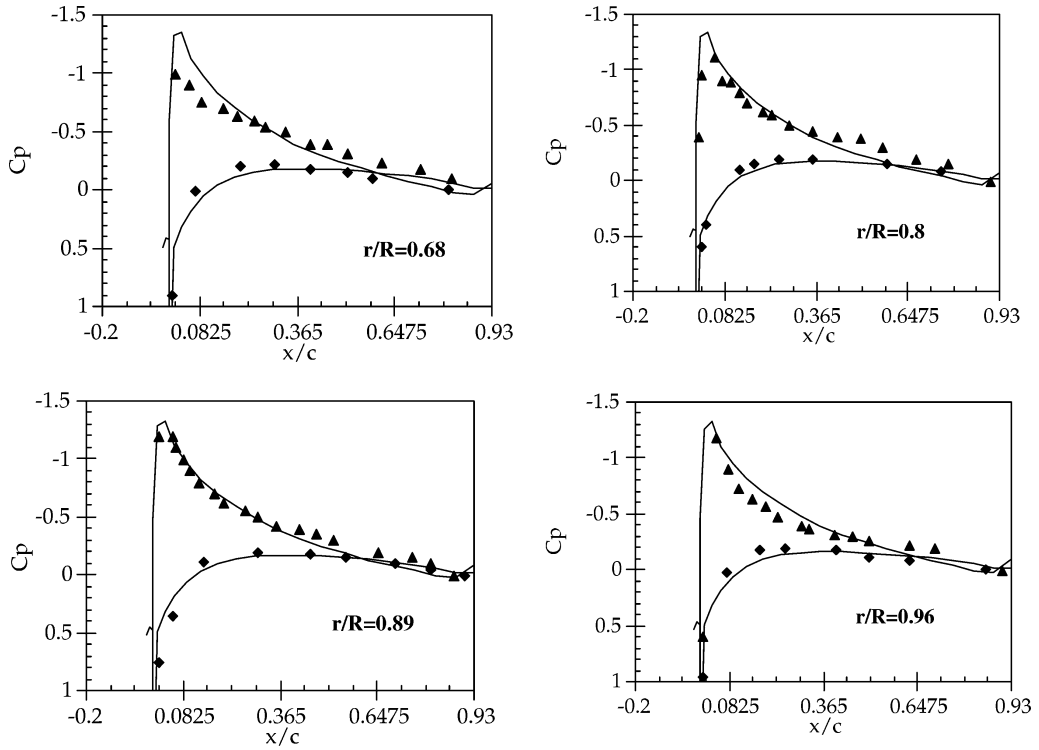

Fig. 5b Comparison of surface pressure distributions at various radial stations for the Caradonna–Tung[13] rotor-blade: ——, N–S Roe–ENO-5 and ◆ and ▲, experiments.

direction, away from the rotor. The case studied was at a freestream tip Mach number of 0.44 and a collective pitch of 8 deg.

Figure 5a shows a comparison of the experimentally observed surface pressure distributions with the computed third-order MUSCL and the ENO-5 results. The ENO-5 scheme used a fixed stencil. The third- and fifth-order results are nearly identical and somewhat overpredict the sectional lift at the span stations plotted. There are two reasons for this overprediction of suction pressures. First, this overprediction is to be expected to some extent because the present simulations in Fig. 5a are inviscid simulations. When the viscous terms are added, the predicted lift levels do come down, closely matching experimental data, as will be discussed later. Next, the grid size used in this simulation is not sufficient enough to capture enough revolutions of the tip vortex and wake vortex sheet. Hence, the wake-induced inflow is not adequately predicted near the inboard regions. This leads to overprediction of suction pressures.

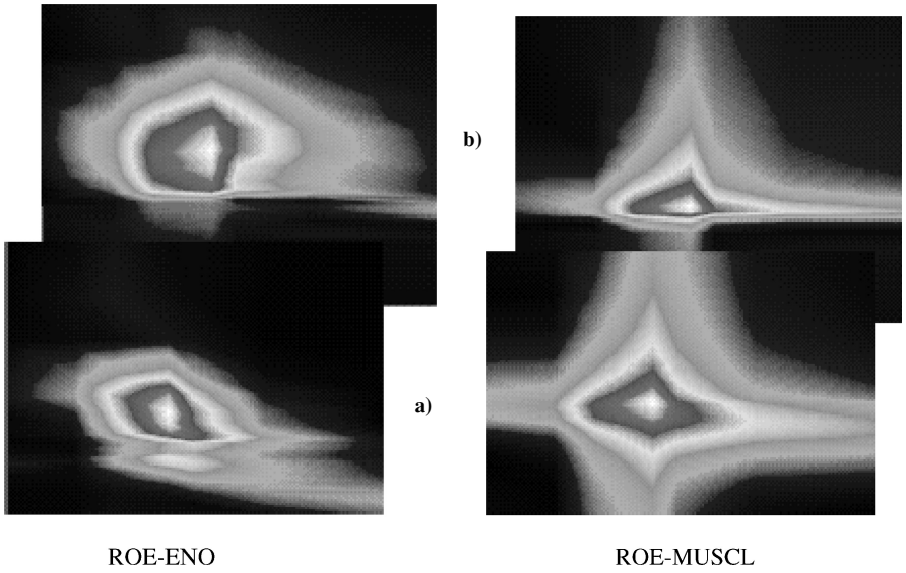

Fig. 6 Comparison of vorticity magnitude contours of the blade-tip vortex in the vicinity of the rotor: a) $x/c = 0.1$ and b) $x/c = 1.0$ behind the trailing edge.

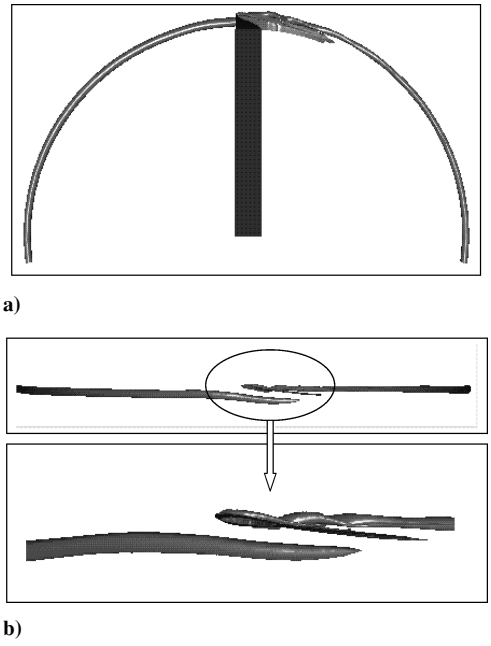

Fig. 7 Vorticity isosurface contours showing the computed tip-vortex structure: a) top view and b) side view.

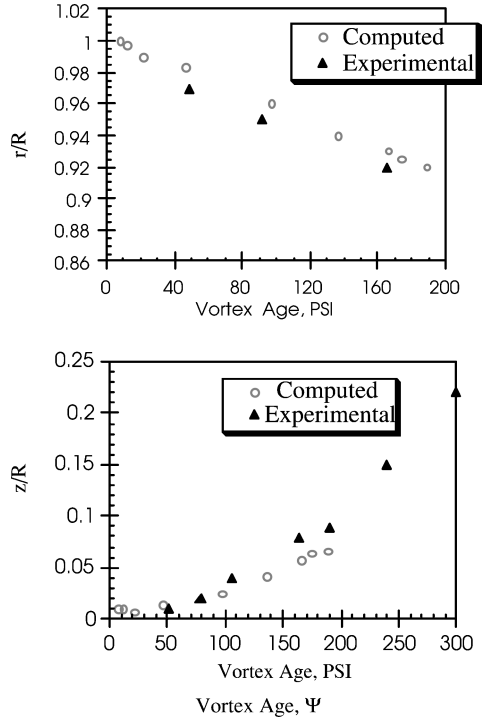

Fig. 8 Comparison of computed and experimental tip-vortex trajectory.

The prediction of inflow velocities near the tip region is more accurate, and hence, a better agreement of the computed C_p values with experiments is seen.

N–S simulations were also done on the baseline grid using the ENO-5 scheme, with a k–ε turbulence model. Surface C_p distributions are shown for typical radial stations in Fig. 5b. A similar N–S simulation done on a denser grid ($217 \times 71 \times 61$) by Srinivasan and Baeder[14] has a comparable surface C_p distribution. In the present work, the suction peak at the inboard stations is not well predicted (but better predicted than the inviscid simulation), but a satisfactory agreement is observed in the outboard regions of the rotor blade.

Figure 6 shows a comparison of the tip vorticity contours between the third- and the fifth-order simulations on the current coarse grid. The tip vortex dissipated away within a 90-deg azimuth downstream of the trailing edge, in both the computations. However, in the vicinity of the trailing edge, as can be seen from Fig. 6, note that the vorticity captured by the fifth-order scheme has a lesser tendency for grid alignment and higher concentration.

The CPU time for the fifth-order scheme is roughly 15% more than the CPU time for the MUSCL scheme. This implementation of the ENO-5 scheme was found to be as robust as the third-order MUSCL scheme. However, the fifth-order scheme was found to be more sensitive to grid skewness, such as near the leading edge of the blade in the H-grid topology. This is to be expected to some extent because the fifth-order scheme uses a larger stencil to construct the cell face fluxes and has lower inbuilt numerical dissipation. Because the current interpolation uses a grid-aligned stencil, any skewness of the grid lines will have some secondary effects (through grid normals, grid metrics, etc.) in introducing errors in the interpolation process. The third-order scheme with its higher numerical dissipation can filter out these oscillations better than the fifth-order scheme.

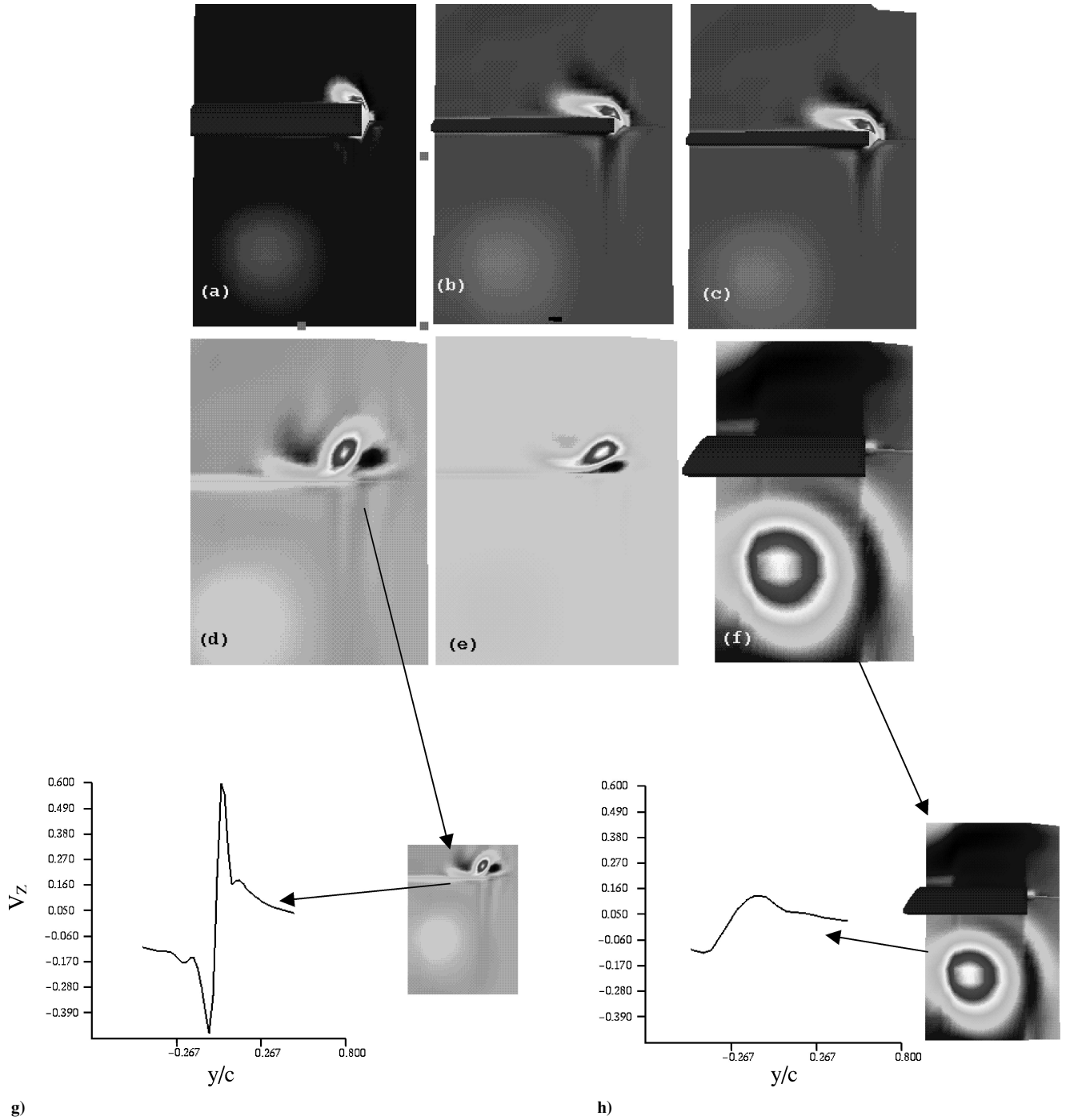

Fig. 9 Vorticity contours showing the evolution of computed (Roe–ENO-5) tip vortex as a function of wake age and peak-to-peak velocity V_z distributions at two different wake ages ∼180 deg apart.

Note that, for the coarse grid used, no perceivable differences could be seen in the predicted surface pressure distributions between the third- and the fifth-order schemes. Although the tip vortex is captured better by the fifth-order scheme when compared to the third-order scheme in the immediate vicinity of the blade, for the mesh size used, the tip vortex dissipates within a few chord lengths behind the trailing edge. Thus, the effective inflow velocity is not predicted accurately enough to reflect in the surface pressure loadings. To assess the full benefits of the fifth-order scheme, a more detailed study of the captured tip vortex is necessary. This problem is addressed in the next section.

Blade-Tip Vortex Numerical Dissipation Characteristics

To resolve the blade-tip vortex better and study the numerical vortex dissipation characteristics, the H grid considered in the preceding section was enhanced, and the ENO-5 simulation repeated for the Caradonna–Tung[13] rotor blade. In this simulation, we look into the velocity distribution across the tip vortex and assess what is needed to resolve a potential BVI in forward flight.

The new grid dimensions of the H-grid system were $120 \times 40 \times 60$ in the streamwise, spanwise, and normal directions, respectively. Figure 7 shows isovorticity contours (top and side views) showing the captured tip vortex. The tip-vortex contraction and descent are very well captured as shown in Fig. 7 over the first 180 deg. Figure 8 shows the comparison of the tip vortex position between the fifth-order simulation and experiments

Figures 9a–9f show the evolution of the vortex over the blade (Figs. 9a–9c, the view from behind the rotor) and its transport underneath the next blade (Figs. 9e and 9f). The vortex strengths are compared by ascertaining the tangential velocity variation across the

vortex at 0-deg azimuth (right off the blade) and at around 180-deg azimuth (as it passes underneath the next blade). The comparison is shown in Figs. 9g and 9h. It is clearly seen that even though the fifth-order scheme (with the current grid structure) has maintained the vortex structure well, the strength itself is well reduced over 180 deg of vortex convection. A much higher fidelity of the vortex is required if interactional effects such as BVI are to be computed with any accuracy. One of the reasons for the tangential velocity dissipation is that the tip vortex in its natural inboard/downward motion moves out of high-density grid region near the blade and out into lower-density grid region in the H grid system. In the next study, we address the question of whether building schemes of further higher-order accuracy will have practical benefits for capturing wake vorticity.

Evaluation of Fifth/Seventh Order ENO Schemes: Wing-Tip Vortex

The design of the H grid and physical motion of the rotor-blade tip vortex results in the tip vortex naturally moving out of high-density grid regions. Every scheme has a rough range of minimal number of grid points that is required across the vortex face to capture the tip vortex without dissipation. To evaluate more accurately the performance metrics of high-order ENO schemes, it is necessary to have finer control of grid points in the path of the tip vortex. For this purpose, a wing-tip-vortex simulation is considered using overset grids. Overset grids allows for better control of how the grid points are distributed.

A NACA0015 blunt-edged wing tested by McAllister and Takahashi[15] was chosen for this study because extensive velocity profile measurements are available from this experiment. To ensure an adequate number of grid points across the vortex face at all downstream locations, a wing grid–vortex grid overset system was used. For the wing grid, a C grid consisting of 121 points in the streamwise direction, 25 points in the spanwise direction, and 31 points in the normal direction was constructed. The vortex grid consisted of a cuboid-shaped, tightly packed grid consisting of 100 streamwise planes, with each streamwise plane consisting of 30×30 grid points. The vortex grid was placed inside the wing grid just behind the trailing edge near the tip. Figure 10 shows the entire overset system. The C grid generates the wing-tip vortex, and the vortex is transferred to the vortex grid in the immediate vicinity of the trailing edge. This overset solution transfer mechanism is enabled using trilinear interpolation, and details of the overset method and its implementation may be found in Ref. 12. The tip vortex is then convected downstream in the vortex grid. This ensures that the tip vortex always stays within computational grids with high grid density.

The wing was set at an angle of attack $\alpha = 12.44$ deg, and the freestream Mach number was set at $M_\infty = 0.18$. Figure 11 shows the tangential (V_z) and axial (V_x) velocity profile comparisons across the tip vortex, in the immediate streamwise locations behind the trailing edge. ENO-5 is compared with the third-order MUSCL solution and experiments. The fifth-order tangential velocity profile V_z agrees very well with the experiments. On the other hand, the

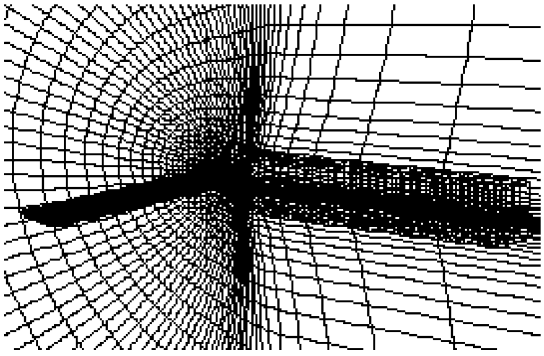

Fig. 10 Overset grid system for wing-tip-vortex study.

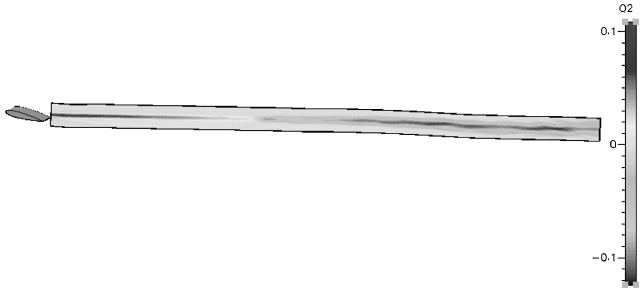

Fig. 12 Streamwise momentum contours across a spanwise section of the vortex grid.

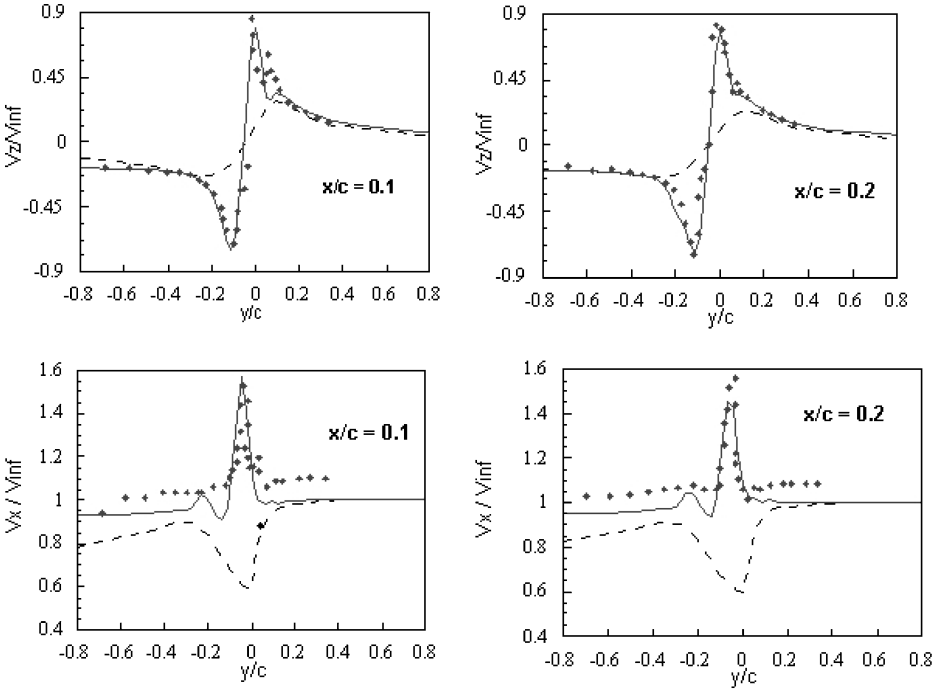

Fig. 11 Comparison of tangential V_Z and axial V_X velocity and distribution across the tip vortex in the immediate downstream vicinity of the wing trailing edge: – – –, Euler third-order MUSCL; ——, Euler ENO-5; and ◆, experiment.

third-order solution produces a diffused profile V_z profile, for the given grid density, and the peaks do not match the experiments.

Predicting the axial velocity field inside a vortex is more difficult because the formation of the axial velocity distribution is a secondary effect and has much sharper spatial gradients. For example, in Fig. 11, even though the third-order solution produced a diffused tangential velocity profile V_z across the vortex, it picked up the correct trend. However, the axial velocity V_x distribution depends, among other factors, on how the tip vortex forms, that is, all blade-tip shapes always produce a tip vortex with a hook-like peak-to-peak tangential velocity distribution, but the axial velocity could either be a deficit or excess depending on the blade tip and flow conditions. As can be seen in Fig. 11, for the given grid density, the third-order scheme is totally off in predicting the axial velocity field, picking up a wrong trend in the distribution. The fifth-order solution not only picks up the right trend, but also agrees reasonably well with experiments in the vicinity of the trailing edge.

Once the vortex formation computation was validated, the ENO-5 solution was used as the feeder to the vortex grid solution to evaluate the dissipative characteristics of high-order schemes for convecting the tip vortex over long distances. At this point, the third-order MUSCL scheme was not considered anymore because ENO-5 has proved superior overall based on the rotor-hover simulation and tip-vortex profile comparisons. ENO-5 and seventh-order ENO scheme (ENO-7) were applied to the vortex grid, and the resulting evolutions of the tip vortex were compared. For the Caradonna-Tung[13] rotor blade, considered in the last section, the blade aspect ratio (AR) is 6.5, and hence, a 180-deg convection would entail $\sim 18(\pi \times \mathrm{AR})$ chord lengths of tip vortex transport. The vortex grid was designed to match this length.

Figure 12 shows the axial momentum component on a cross section of the vortex. It is instructive to compare the axial velocity/momentum component because it has a much steeper gradient and is, hence, more difficult to capture without numerical diffusion for a given grid. The captured vortex has a positive axial momentum (jet-like) till around the halfway mark of the 18 chords. Then it switches over to a negative axial momentum, exhibiting a wakelike behavior. A real physical vortex may exhibit a similar behavior due to viscosity.

However, the current simulation is inviscid, and such a transition is incorrectly triggered by the dissipation in the numerics. The axial velocity component in a realistic vortex (over a wing or a rotor) plays an important role in the determination of the vortex structure. A closer look at the variation of the axial and tangential velocity components reveals the need for accurately capturing the axial velocity. Figures 13a–13c show the axial and tangential momentum components across the vortex at the 5, 50, and 100% mark of the length of the vortex grid, respectively.

The fifth-order scheme captures the tangential velocity variation with 8–10 grid points across the vortex core, but the axial velocity tends to get dissipated when the convection distances are more than 10 chord lengths. If the axial velocity dissipates (due to numerical dissipation) below zero, it switches to a wakelike structure, changing the peak-to-peak tangential velocity variation to a different lower value.

ENO-7 was next applied to the vortex grid. The computation inside the vortex grid is uniformly seventh-order accurate, using one-sided stencil shift near the boundaries. Of direct interest are the three queries, 1) stability, 2) increased cost of computation per iteration, and 3) the payoffs in terms of the ability of ENO-7 to resolve the vortex.

Figure 14 shows the axial momentum contour across a spanwise plane cutting the vortex. The axial momentum variation is captured with very little dissipation over the entire ~ 18 chord lengths. The axial momentum contours appear diminished in patches toward the 70% mark and the 90% mark. This is because the vortex "wiggles" sideways and the maximum does not always stay in the same plane. Figures 15a–15c compare the axial and tangential velocity variation at the 5, 50, and 100% mark of the length of the vortex grid, respectively. The axial component has very little dissipation, and the tangential component has no noticeable dissipation. The seventh-order scheme requires around five points across the vortex face to capture both the axial and tangential velocity accurately. The stability of ENO-7 was not affected, for the Cartesian vortex grid. The same time stepping that was applied using the ENO-5 computation was retained for the ENO-7 computation.

As a further demonstration of high-order vortex capturing, the ENO-7 simulation was repeated with the vortex grid extended to 50 chord lengths. The streamwise number of points was increased to 300 to keep the streamwise grid density approximately the same. The spanwise grid point density distribution was retained at 30×30. All of the other flow conditions were identical to the simulations described earlier. The length of the vortex grid roughly represents 3–4 half-revolutions of rotor-tip vortex, for a rotor of aspect ratio 6. Figure 16 shows the axial momentum isosurface contour inside the vortex, over the 50 chord lengths of simulation. The axial and tangential momentum variation across the vortex at $x/c = 2$, 25, and 50 are also shown in Fig. 16. The ENO-7 scheme captures the vortex without any noticeable dissipation. In summary, the metrics that characterize the capability to capture/convect vortices are compared in Table 1 for MUSCL, ENO-5, and ENO-7.

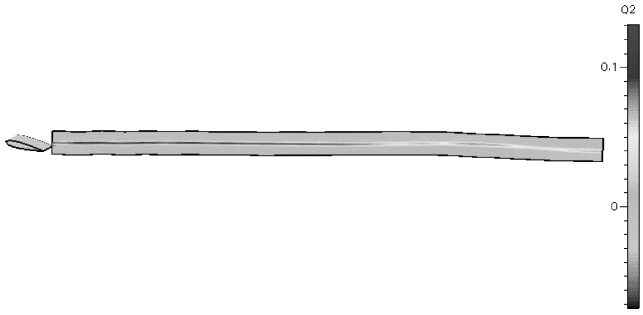

Fig. 14 Axial momentum contours across a spanwise section of the vortex grid.

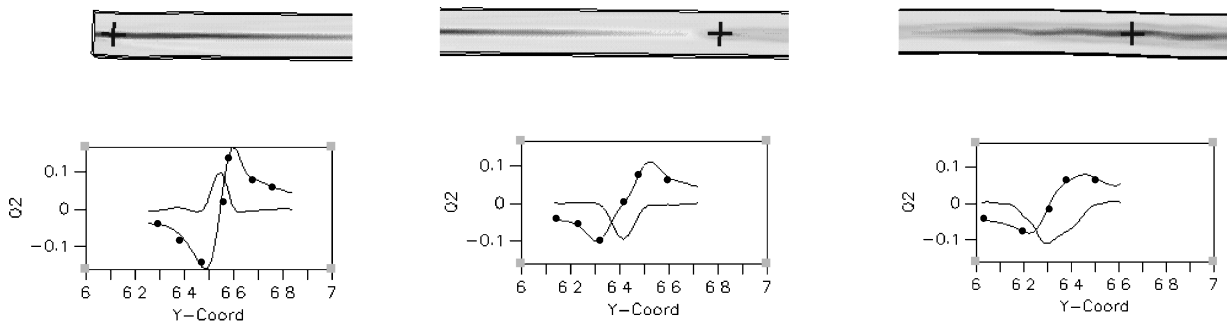

a) x/c = 1.0 **b) x/c = 9.0** **c) x/c = 15.0**

Fig. 13 Comparison of axial and tangential momentum variation across the vortex at several streamwise stations: ——, axial momentum and ●, tangential momentum.

Table 1 Comparison of vortex-capturing metrics[a]

Scheme	CPU time/iteration, s	Grid points required across vortex for resolution	Stability
MUSCL	8.3	18–20	Baseline
ENO-5	13.5	8–10	Mild time-stepping restrictions nonorthogonal grids (H-type meshes)
ENO-7	17.2	4–6	Severe time-stepping restrictions on nonorthogonal grids (H-type meshes)

[a]With ~200,000 grid points, 3 subiterations per iteration, DEC-Alpha 500 workstation.

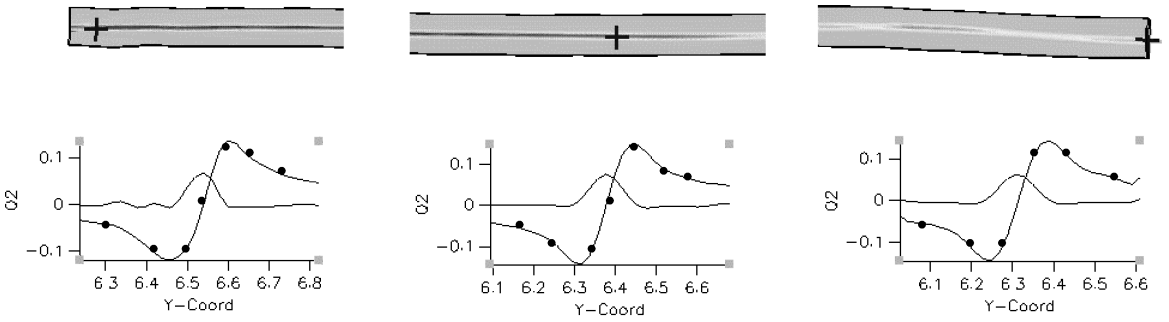

a) x/c = 1.0 **b) x/c = 9.0** **c) x/c = 18.0**

Fig. 15 Comparison of axial and tangential momentum variation across the vortex at several streamwise stations.

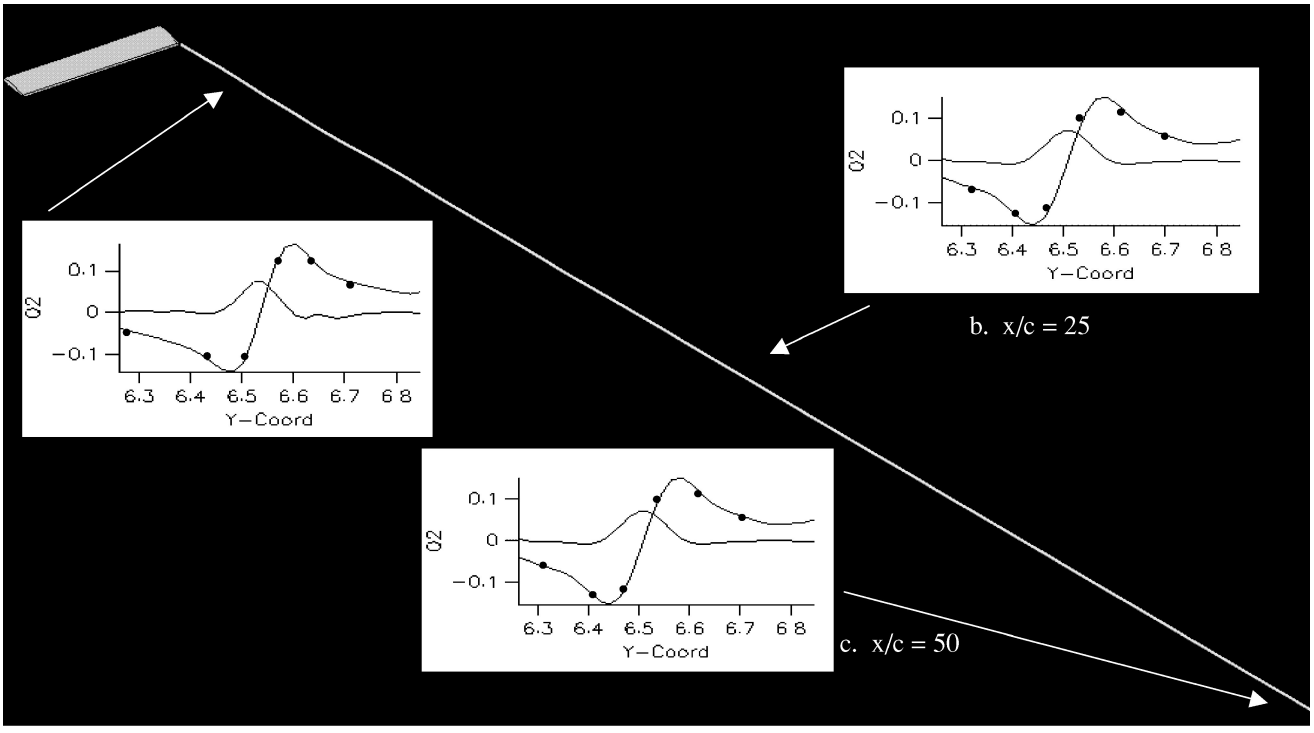

Fig. 16 Isosurface of axial momentum, showing the tight tip vortex structure and axial and tangential momentum variations across the tip vortex at various streamwise stations: ——, axial momentum and ●, tangential momentum.

Conclusions

The advantages of ENO-based high-order methods in capturing wake vorticity were outlined. An ENO-7 scheme has been demonstrated to capture tip vortices using around five grid points across the vortex and is a likely candidate for computing rotor-blade wakes using Cartesian background grids. One of the drawbacks with ENO schemes is that they are not compact, and hence, a wide stencil of information is required to construct the high-fidelity solution. This becomes a problem when large-scale simulations are broken into parts and distributed over a computing network, making it necessary to have sufficient overlap between the grid parts to construct uniformly high-order accurate solution. One possible solution is to let the natural adaptive underlying methodology of ENO to construct one-sided high-order solutions near the grid boundaries created due to a distributed grid partition. Further research is needed to refine ENO high-order methods for three-dimensional rotorcraft wake computations to arrive at an optimal scheme applicable uniformly in multiple grid settings.

Acknowledgments

Parts of results presented in this paper were done under NASA Small Business Innovation Research Contract NAS2-14226. The

National Rotorcraft Technology Center supported L. N. Sankar. N. Hariharan would also like to thank Z. J. Wang of Michigan State University and Roger Strawn of NASA Ames Research Center for the various discussions, during this effort.

References

[1]Srinivasan, G. R., and Ahmad, J. U., "Navier–Stokes Simulation of Rotor-Body Flowfield in Hover Using Overset Grids," Confederation of European Aerospace Studies, Paper C15, *CEAS 19th European Rotorcraft Forum*, Sept. 1993.

[2]Strawn, R. C., Biswas, R., and Garceay, M., "Unstructured Adaptive Mesh Computations of Rotorcraft High-Speed Impulsive Noise," *Journal of Aircraft*, Vol. 32, No. 4, 1995, pp. 754–760.

[3]Duque, E. P. N., and Srinivasan, G. R., "Numerical Simulation of a Hovering Rotor Using Embedded Grids," *Proceedings of the 48th Annual Forum of American Helicopter Society*, AHS, Vol. 2, Alexandria, VA, May 1992.

[4]Duque, E. P., "A Structured/Unstructured Embedded Grid Solver for Helicopter Rotor Flows," *Proceedings of the 50th Annual Forum of American Helicopter Society*, Vol. 2, Alexandria, VA, May 1994.

[5]McCroskey, W. J., "Wake Vortex System of Helicopters," AIAA Paper 95-0530, Jan. 1995.

[6]Harten, A., Engquist, B., Osher, S., and Chakravarthy, C. R., "Uniformly High Order Accurate Essentially Non-oscillatory Schemes III," *Journal of Computational Physics*, Vol. 131, No. 1, 1997, pp. 3–47.

[7]Hariharan, N., and Sankar, L. N., "Higher Order Numerical Simulation of Rotor Flow Field," *American Helicopter Society Forum and Technology Display*, Paper 19940511, May 1994.

[8]Hariharan, N., and Sankar, L. N., "Application of ENO Schemes to Rotary Wing Problems," AIAA Paper 95-1892, June 1995.

[9]Hall, C. M., and Long, L. N., "High-Order Accurate Simulations of Wake and Tip Vortex Flowfields," *Proceedings of the 55th Annual Forum of American Helicopter Society*, Vol. 2, Alexandria, VA, May 1999.

[10]Tang, L., and Baeder, J. D., "Improved Euler Simulation of Hovering Rotor Tip Vortices with Validation," *Proceedings of the 55th Annual Forum of American Helicopter Society*, American Helicopter Society, Vol. 2, Alexandria, VA, May 1999.

[11]Hariharan, N., "A First-Principles Based High Order Discontinuous Galerkin (DG) Methodology for Rotorcraft Flowfield Studies," NASA Small Business Innovation Research Phase-I Rept. NAS2-98062, CFD Research Corp., Huntsville, AL, Oct. 1998.

[12]Hariharan, N., and Sankar, L. N., "Unsteady Overset Simulation of Rotor-Airframe Interaction," *Journal of Aircraft*, Vol. 40, No. 4, 2003, pp. 662–674.

[13]Caradonna, F. X., and Tung, C., "Experimental and Analytical Studies of a Model Helicopter Rotor in Hover," *Vertica*, Vol. 5, No. 2, 1981, pp. 149–161.

[14]Srinivasan, G. R., and Baeder, J. D., "TURNS: A Free Wake Euler/Navier–Stokes Numerical Method for Helicopter Rotors," *AIAA Journal*, Vol. 31, No. 5, 1993, pp. 959–962.

[15]McAlister, H. W., and Takahashi, R. K., "NACA0015 Wing Pressure and Trailing Vortex Measurements," U.S. Army Aviation Systems Command, TR-91-A-003, NASA TP 3151, Nov. 1991.